

Choosing the metal oxide for an electro-chemo-mechanical actuator working body

Evgeniy Makagon^a, Junying Li^b, Yuanyuan Li^b, Ellen Wachtel^a, Anatoly I. Frenkel^b, Igor Lubomirsky^{a,*}

^a Dept. of Molecular Chemistry and Materials Science, Weizmann Institute of Science, Israel

^b Dept. Materials Science and Chemical Engineering, Stony Brook University, NY, USA

ARTICLE INFO

Keywords:

Electro-chemo-mechanical actuation
Electromechanical response
Mixed ionic electronic conductivity
MEMS

ABSTRACT

The term “electro-chemo-mechanical (ECM) effect” describes mechanical deformation driven by an electrochemical reaction. Recently, an all-solid-state ECM device operating at room temperature was demonstrated. The device comprised a 20 mol% Gd-doped ceria (20GDC) self-supported electrolyte membrane placed between two mixed ionic/electronic conducting (MIEC) working bodies (WBs) constructed with TiO_x/20GDC nanocomposites. Actuation derived from volume change occurring upon oxidation/reduction of the WB. This raised the question of whether or not metal oxides other than TiO_x could be valuable components in MIEC nanocomposites functioning as WBs in ECM actuation. Here we examine the microstructure, crystal phase, oxidation state, chemical composition and ECM functionality of V-, Nb-, Mo-, Cu- and Ag-oxide/20GDC composite WBs prepared by co-sputtering. Of these, only the V-based composite was shown to be suitable for ECM actuation. According to X-ray absorption spectroscopy, the composition of the nanocomposite corresponds to VO_x/20GDC. Electrical characterization suggests that the formation of several coexisting VO_x nano-oxide phases is responsible for the longer response times as compared to TiO_x/20GDC WBs. ECM actuation demonstrated in the V-based system does indicate that composite WB based ECM is not unique to Ti and that this type of actuation constitutes a significant contribution to development of microelectromechanical systems.

1. Introduction

Electro-chemo-mechanical (ECM) coupling produces dimensional change in a solid as a result of compositional change driven by an electrochemical reaction [1–3]. The ECM effect is observed in a large variety of materials used for energy storage or conversion and is generally considered to be highly detrimental. As an example, Li incorporation in, and extraction from, the electrodes of a Li-ion battery is accompanied by a large volume change and, consequently, by mechanical strain [4–8]. In such devices, the strain induced by the ECM effect leads to cracking, delamination and eventual failure [7,9,10]. However, ECM coupling has a positive side as well. An ECM mechanical actuator, first demonstrated by Swallow et al., [11] at 550 °C, requires two basic components: a working body (WB), which undergoes change in composition; and an ion conducting electrolyte, adjacent to the WB, functioning as a reservoir in which the ions, incorporated or extracted from the WB, are stored. In the device described in ref. [11], the WB was

a thin layer of Ce_{0.9}Pr_{0.1}O_{1.95-δ} deposited on a Y-stabilized zirconia electrolyte. While validating the ECM actuation concept, the displacements produced were too small for practical use.

We have recently demonstrated that ECM actuation can be achieved at room temperature in an all solid state device comprising a 20 mol% Gd-doped ceria (20GDC) self-supported electrolyte membrane placed between two WBs undergoing change in volume upon oxidation or reduction (Fig. 1a). A nanocrystalline TiO_x/20GDC mixed ionic-electronic conducting (MIEC) composite was used as the WB, producing response time of a few seconds [12]. The effective oxygen diffusion coefficient in the composite was $\approx 10^{-15}$ cm²/s, which is 1–2 orders of magnitude larger than in the 20GDC electrolyte (10^{-16} – 10^{-17} cm²/s [13]). Comparing the ECM response times achieved in refs. [12, 14] permits us to conclude that the accelerated diffusion was likely to have been achieved due to more rapid interfacial transport [15–18] in the composite, which results in electrochemical reactions occurring throughout a large fraction of the WB volume. Nanocrystalline

* Corresponding author.

E-mail address: igor.lubomirsky@weizmann.ac.il (I. Lubomirsky).

<https://doi.org/10.1016/j.ssi.2022.115913>

Received 11 November 2021; Received in revised form 18 March 2022; Accepted 24 March 2022

0167-2738/© 2022 Published by Elsevier B.V.

composites, prepared by co-sputtering, constitute a significant improvement over WBs with direct Ti metal-20GDC contacts [14]. The ECM response in the latter depends on the formation and subsequent reduction of a thin layer of Ti-oxide at the interface between the Ti contact and the 20GDC electrolyte [14]. There, the ECM response rapidly saturates due to slow diffusion through the TiO_x layer. By comparison, during co-sputtering of the nanocomposite WB, Ce oxidizes Ti, thereby producing a +3/+4 mixed valence state both for Ti (ratio 0.2/0.8) and for Ce (ratio 0.4/0.6) [12] providing the necessary constituents for the oxidation and reduction of Ti, without compromising the oxygen diffusion through the WB. Indeed, analysis of the mechanical response revealed that oxidation/reduction of Ti was responsible for the ECM actuation.

Successful demonstration of ECM actuation with [Ti oxide\20GDC nanocomposite] WB-based devices raised the question of whether or not metal oxides other than TiO_x could be valuable components in MIEC nanocomposites functioning as WBs in ECM actuation. In the following, we consider criteria for the choice of metal oxides for the composite WBs and present the results of structural and electromechanical characterization investigating their suitability for ECM actuation.

2. Choice of metal-oxides for a composite WB

Two necessary, but not sufficient, criteria for the choice of metal-oxide for the ECM WB composite are: (i) the metal should support at least two oxidation states; and (ii) the oxides corresponding to these oxidation states must not be insulating. The latter criterion stems from the fact that if an electrochemical reaction produces an electrical insulator, the kinetics of the reverse reaction are very slow. Three candidates, in which either the 3d or 4d subshell is partially filled in the ground state, were selected for the current study: V ($3d^3, 4s^2$), Nb ($4d^4, 5s^1$) Mo ($4d^5, 5s^1$). Cu ($3d^{10}, 4s^1$) and Ag ($4d^{10}, 5s^1$) were investigated as well. Of these, vanadium appears to be the most promising: at room temperature, it supports a number of oxidation states between +2 and +5 with corresponding oxides: VO (cubic), V_2O_3 (corundum), VO_2 (monoclinic), and V_2O_5 (orthorhombic). Moreover, vanadium forms a large variety of mixed valence oxides (V_6O_{13} , V_8O_{15} , V_7O_{13} , V_6O_{11} , etc.), with different crystallographic structures [19]. Under ambient conditions, V-oxides demonstrate electronic conductivity ranging from 10^{-7} S/cm for V_2O_5 to 10^2 S/cm for VO [20]. Niobium forms a series of oxides NbO, NbO_2 , Nb_2O_5 with a single oxidation state +2, +4 or +5 [21–24] and a set of mixed valence oxides, e.g., $\text{Nb}_{22}\text{O}_{54}$ and $\text{Nb}_{12}\text{O}_{29}$ [22,24]. Conductivity of the Nb oxides is dependent on stoichiometry

and varies over several orders of magnitude: 10^{-6} - 10^2 S/cm [22,24,25]. Molybdenum exhibits two major oxidation states, +4 and +6, and the corresponding oxides can be readily oxidized/reduced. MoO_x phases, $2 < x < 3$ [26,27], are not insulating: MoO_3 is a semiconductor with conductivity $>10^{-7}$ S/cm [28,29]; at the other extreme is metallic MoO_2 , with conductivity up to 10^4 S/cm [30,31]. Copper supports two oxidation states, +1 and +2, forming oxides Cu_2O , Cu_4O_3 and CuO , which can readily transform from one to the other [32]. Thin films of copper oxides are reasonably conductive, $(1-9)\cdot 10^{-3}$ S/cm [33–36]. Silver primarily supports oxidation state +1, with corresponding oxide Ag_2O ; however, under strongly oxidizing conditions, oxidation state +2 (or a mixture +1 and +3) with AgO stoichiometry is known. The Ag_2O phase is the most stable [37] and is reasonably conductive, $3\cdot 10^{-3}$ S/cm [38].

3. Experimental

Sample preparation. ECM actuation devices based on nanocomposite WBs with 20GDC as the electrolyte were fabricated according to the process described in ref. [12] and schematically represented in Fig. 1b. Briefly, a 7 layer film stack was deposited using DC (metal) and RF (20GDC) magnetron sputtering (ATC Orion Series Sputtering System, AJA International Inc.) on a *p*-doped (100) 2", 285 μm thick Si wafer. The stack comprised (i) an Al stress relief layer (150 ± 20 nm); (ii) metal bottom contact (depending on the metal in the composite) ($250 \text{ nm} \pm 20$ nm); (iii) bottom composite layer (100 ± 20 nm); (iv) electrolyte layer (1.5 ± 0.2 μm); (v) top composite and metal layers (See Table 1 for deposition conditions). An Al capping layer (150 ± 20 nm) was deposited on top of the metal contact, thereby isolating the contact and the composite from the external environment, and thus preventing any dependence on relative humidity (15–85%) as well as on oxygen

Table 1

Deposition conditions for the thin film multilayer stack of the actuation device. Composite layer deposition conditions are metal dependent and detailed in Table 2. Top and bottom metal contact and composite layers were deposited under the same conditions.

Material	Pressure (mTorr)	Gas flow (SCCM)	Power (W)	Temperature ($^{\circ}\text{C}$)
Al	3	Ar: 30	DC: 200	25
Metal contact	3	Ar:30	DC:150	25
20GDC	20	Ar:30 O ₂ :3	RF: 100	120

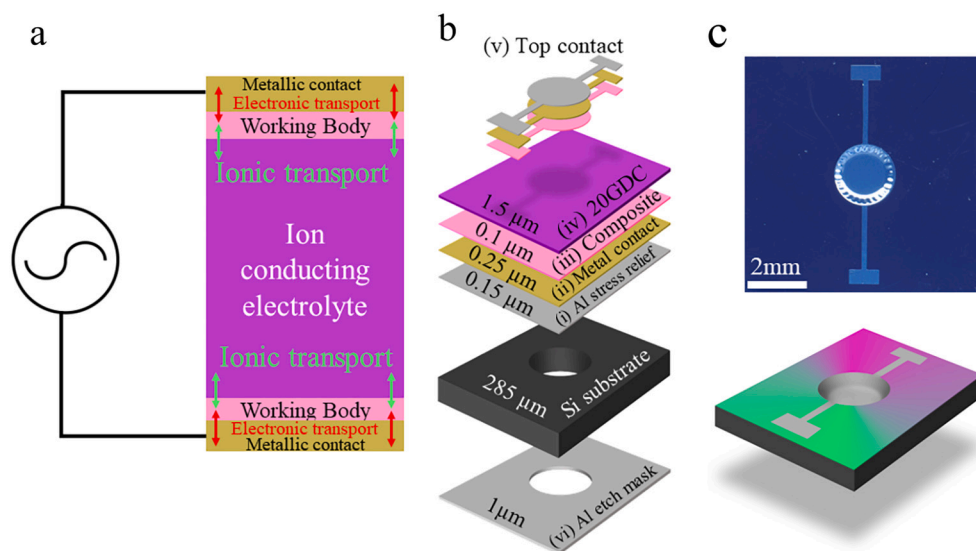


Fig. 1. (a) Schematic representation of an ECM actuation device, describing the components and mechanisms required for its operation. (b) Practical implementation of the design concept; the complete layer stack is detailed. The top contact and substrate removal are performed by lithographic patterning, wet chemical metal etch and reactive ion dry etching. (c) Assembled device (bottom); optical micrograph of the actuator showing the buckling pattern of the self-supported multilayer membrane (top).

partial pressure. The top contact was patterned into a circular shape with two legs using UV lithography (MA6 BSA Mask Aligner, Karl Suss) and dry reactive ion etching (730 SLR, Plasma-therm). (vi) 1 μm thick aluminum mask was deposited on the backside of the Si wafer and circular holes were patterned in the mask. Dry reactive ion etching (STPS Technologies, KLA-Tencor) was used to remove the silicon through the circular holes in the aluminum mask using a Bosch process producing a self-supported, 7-layer, tethered membrane with total thickness $\sim 2\text{--}2.5\ \mu\text{m}$. Finally, the wafer was cut into $8 \times 8\ \text{mm}^2$ samples (Fig. 1c).

X-ray absorption spectroscopy (XAS). For XAS measurements, the metal (oxide)/20GDC composites were deposited by co-sputtering onto SiO_2 substrates with 200 nm Al stress relief layers. Deposition conditions for the composite layer are detailed in Table 2. Identification of the oxidation state and local structure around the metal ions of the composite layers (including Ce and Gd) by XAS was performed at beamlines 7-BM (V-oxide/20GDC) and 8-ID (Mo-oxide/20GDC, Ag-oxide/20GDC, Cu-oxide/20GDC, and 20GDC thin films), National Synchrotron Light Source II, Brookhaven National Laboratory, and at beamline 20-BM-B (Nb-oxide/20GDC), Advanced Photon Source, Argonne National Laboratory. Data were collected in the fluorescence mode.

Composite microstructure and crystallography. Microstructure of the composite WBs was examined by scanning electron microscopy (SEM, Sigma FEG, Zeiss, 3 kV accelerating voltage). Energy dispersive spectroscopy (EDS, XFlash 6–60, Bruker, at 25 kV acceleration voltage) was used to determine the elemental composition of the composite layers. Crystallography of the nanocomposites was determined by X-ray diffraction (XRD, Rigaku TTRAX III, Bragg Brentano, $\Theta/2\Theta$ mode, scan rate $2^\circ/\text{min}$).

Electrical characterization. Electrical characterization of the ECM actuators was performed using cyclic voltammetry (CV, B2912A Precision Source/Measure Unit, Keysight Technology Inc., internal ammeter resistance $< 200\ \Omega$) and impedance spectroscopy (IS, ZG-4 with Alpha-A modular measurement system, Novocontrol Technologies GmbH & Co. KG). Temperature dependent measurements were performed in the $25\text{--}100\ ^\circ\text{C}$ range using a heating resistor connected to an auto tuning temperature controller (PTC10, Stanford Research systems, PT100 thermometer).

Electromechanical characterization. Electromechanical characterization was performed using a custom-made, optical system based on dynamical autofocusing [39] (See Supplementary Information for more details). Voltage was applied to the bottom contact with a function generator (Rigol, DG4062) and current was monitored using a precision source/measure unit (B2912A, Keysight Technology Inc.).

4. Results

4.1. Vanadium-oxide based nanocomposite

The XRD pattern of the V-oxide/20GDC composite displays three broad diffraction maxima, as well as the sharp peaks of the Al stress-relief layer (Fig. 2a). The dominant maximum at $2\theta = 30 \pm 0.5^\circ$ is identified as the (111) diffraction peak of the 20GDC component,

Table 2

Deposition conditions for metal oxide/20GDC composites deposited on SiO_2 substrates with Al stress relief layer. All samples were deposited at room temperature, 20 mTorr chamber pressure, 30 SCCM Ar flow. 20GDC power was 100 W RF. All samples were then annealed for 4 h at $430\ ^\circ\text{C}$ in vacuum. Metal content was measured using EDS.

Metal	DC power (W)	Metal content (At.%)
Nb	100	56 ± 1
Mo	100	63 ± 2
V	70	28 ± 0.5
Cu	50	58.6 ± 0.5
Ag	18	52.4 ± 0.8

$\text{FWHM} = 4.25 \pm 0.2^\circ$. The very large peak widths, when compared to bulk 20GDC, attest to the very small crystallite size [40]. The SEM image of the V-based composite shows a dense nano-grained structure with “feature” size $21 \pm 4\ \text{nm}$ (Fig. 5, Fig. 2b). Since these features are much larger than the crystallite size determined by XRD, these must not be single crystal grains but rather grain agglomerates, as was also observed previously for Ti [12]. The V K-edge X-ray absorption near edge structure (XANES) spectrum [41] revealed the presence of a strong pre-edge peak, indicative of a locally non-centrosymmetric environment. Similar peaks were observed for Ti in Ti/20GDC composites [12] as well as in quasi-amorphous BaTiO_3 [42]. Recently, it was reported that identification of V structural motifs and oxidation states can be made on the basis of the intensity and position of the pre-edge peak [41]. The V oxidation state in the V-oxide based composite was shown to be a $+4/+5$ mixture [41]. The Gd L_3 edge XANES spectrum is unchanged from that observed for Gd-doped ceria (oxidation state $+3$), as expected (Supplementary, Fig. S1a). The oxidation state of Ce is a $+3/+4$ mixture (Fig. S1b). We conclude that, even though the composite was deposited with Ar as the sputtering gas, most of the V metal becomes oxidized during deposition.

V-oxide/20GDC composite WB-based ECM devices display a first-harmonic mechanical response, which closely follows the electrical driving current (Fig. 2c). The response was shown to be asymmetric (Fig. 2d), i.e. upon initial bias application, the upward displacement is larger than the downward displacement. This was attributed to the fact that, although the voltage applied to the device is symmetric, the current produced is asymmetric. Since ECM actuation is current-driven, asymmetric currents (Fig. 2c) produce asymmetric mechanical response. Current asymmetry, readily visible as asymmetry in the I-V curves (Fig. 3a-b), most likely originates during sample fabrication. The bottom composite layer is heated to $120\ ^\circ\text{C}$ for 20 h during 20GDC layer deposition. On the other hand, the top composite layer is deposited at room temperature after the substrate has cooled. This produces an initial difference in the chemical potential of oxygen between the top and bottom composite WBs. Repeated application of alternating voltage or thermal cycling leads to eventual equilibration of the oxygen chemical potential and with time, the mechanical response does become symmetric (Fig. 2d). Similarly, the resistance to fatigue examined by cycling the device at 6 V, 1mHz for 105 h (378 cycles) shows that, following an initial decrease in the response, displacement stabilizes after ≈ 72 cycles (Fig. 2e). The amplitude of the response decreases monotonically as $1/f$ on a log-log scale between 10mHz–500 μHz with slope $\sim 1\ \mu\text{m}/\text{Hz}$ (Fig. 2f) This is similar to what was observed for Ti oxide/20GDC WBs [12] and suggests that the mechanical response is a diffusion-related process. Although the amplitude of the observed displacement can reach values comparable to those of Ti oxide/20GDC WBs, they are achieved at much lower frequencies. For example, 1 μm displacement is achieved at 10mHz for Ti oxide/20GDC WBs and at 1mHz for V oxide/20GDC WBs.

A Nyquist plot of the complex impedance (Fig. 3c) of the multilayer ECM device contains a single, depressed high frequency arc and a low frequency constant phase element. The arc was successfully fit to a semi-circle giving $R = 97.2 \pm 0.3\ \text{M}\Omega$ ($R_{\text{adj}} = 0.99989$), which is 2 orders of magnitude larger than the resistance measured for a thin 20GDC layer [43]. The presence of the low frequency, constant phase element is consistent with the presence of ion diffusion (Warburg impedance); however, it appears at $f \leq 1\ \text{mHz}$, which is more than an order of magnitude lower than for Ti oxide/20GDC WBs.

Cyclic voltammetry does not produce unambiguous evidence for a diffusion-limited chemical reaction at room temperature. Voltage sweep rate as slow as 16 mV/s does not produce discernible current peaks in the (-10 V) to (+10 V) potential window (Fig. 3a). Only if the device is heated to $55\ ^\circ\text{C}$, current peaks become visible for both the positive and negative bias ranges (Fig. 3) with significant asymmetry between the current directions. The dependence of the peak current on the square root of the sweep rate marginally deviates from linear (Fig. 3d),

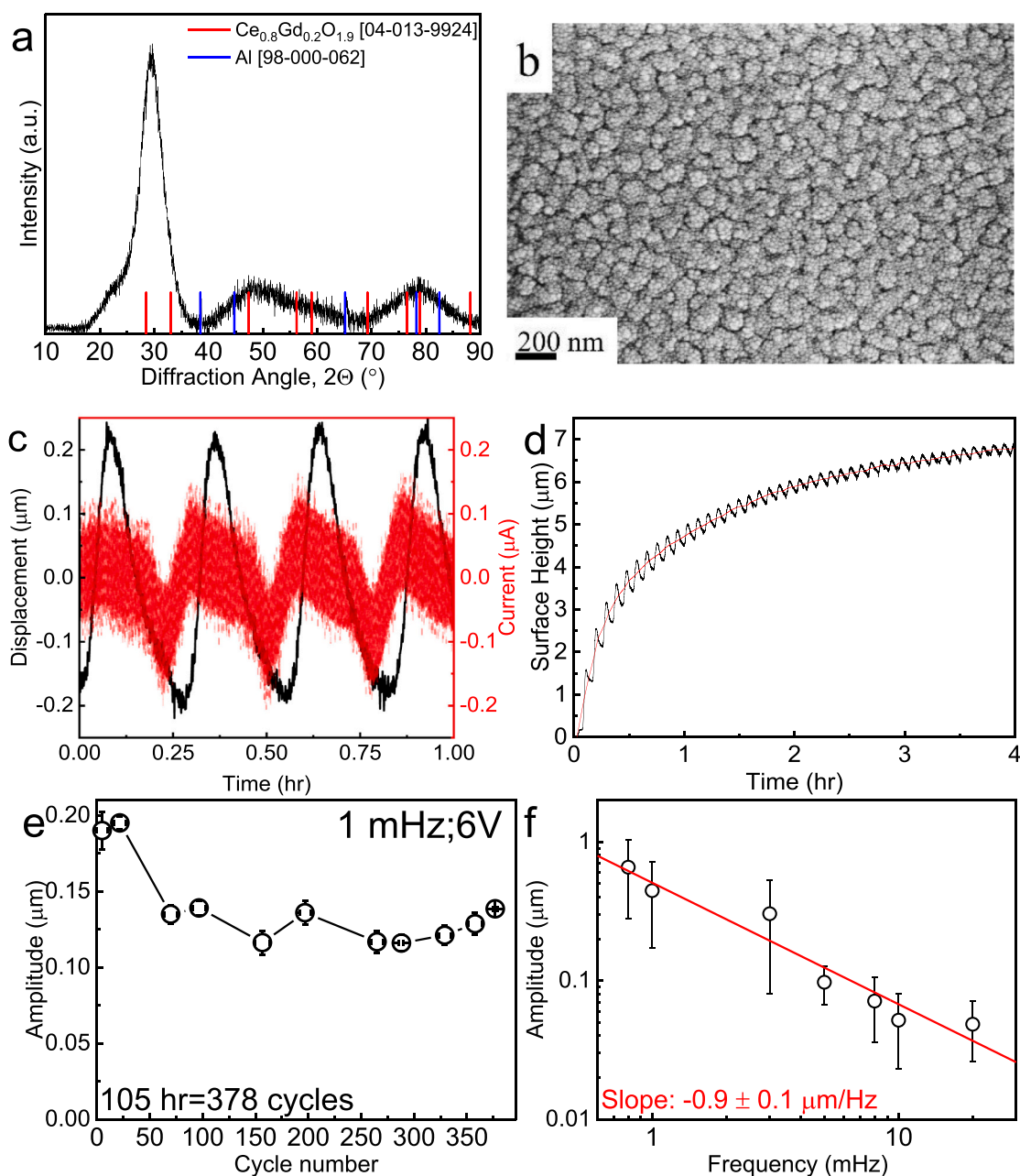


Fig. 2. V oxide/20GDC composite characterization. (a) X-ray diffraction pattern and (b) High resolution SEM micrograph. Aggregate feature size of 21 ± 4 nm was determined by the lineal intercept method. (c) Vertical displacement, measured by an auto-focusing optical technique, of a V-oxide/20GDC composite WB based device driven at 8 V, 1mHz. (For a more detailed description of the technique, see Supplementary Information). The measured current is also indicated. Displacement was centered around zero by removing the background drift. First harmonic response is demonstrated, consistent with ECM. (d) The raw, untreated signal measured for the V oxide/20GDC composite WB based device driven at 8 V, 3mHz. An asymmetric response causes the device to deflect upwards. The red curve identifies the background subtracted to achieve the zero-centered displacement demonstrated in (c). (e) Fatigue characterization of the V oxide/20GDC composite WB based device. The device was cycled at 1 mHz, 6 V for 150 h. An initial decrease in amplitude was observed, with stable amplitude demonstrated after 72 cycles. (f) Log-log plot of the amplitude of the ECM response vs. bias frequency at 8 V. Response amplitude scales with the inverse frequency giving a slope of $-0.9 \pm 0.1 \mu\text{m}/\text{Hz}$. (For interpretation of the references to colour in this figure legend, the reader is referred to the web version of this article.)

rendering applicability of the Randles/Sevcik equation problematic [44]. However, even assuming that this equation holds, the slope corresponds to an oxygen diffusion coefficient ranging between $(3 \pm 1) \cdot 10^{-18} \text{ cm}^2/\text{s}$ at room temperature to $(1.1 \pm 0.8) \cdot 10^{-11} \text{ cm}^2/\text{s}$ at 100°C (Fig. 3e). These values are 3 orders of magnitude lower than those measured for the Ti oxide/20GDC composite [12] and 2 orders of magnitude lower than bulk 20GDC [13]. The voltammograms have two self-crossing points in the range of 0.3-4 V; and combined with the fact that the peak current increases with decreasing sweep rate [45], a

memory effect (memristance) is suggested. This effect may be attributed to the fact that, in contrast to Ti oxide/20GDC composite devices, where Ti transitions between two conductive oxides, in V oxide the oxidation state transition between +4 to +5 is accompanied by an ambient temperature, metal/insulator transition [46], the latter being poorly conductive [20].

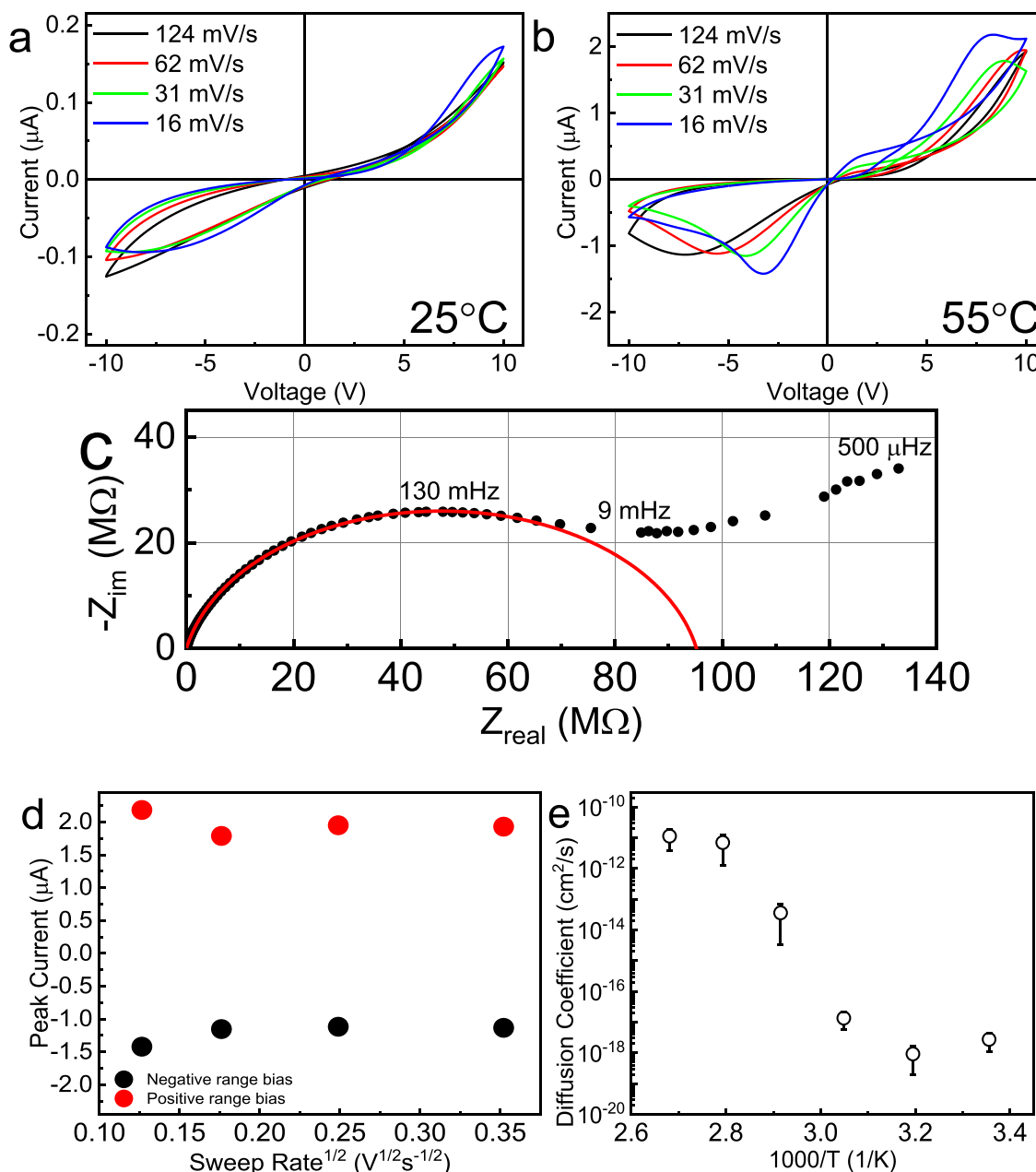


Fig. 3. Electrical characterization of V oxide/20GDC composite WB based device. (a) Cyclic voltammograms measured at room temperature with sweep rate between 16 and 124 mV/s. No distinct current peaks can be detected in the (-10 V) to (+10 V) potential window; some asymmetry is observed. (b) Cyclic voltammogram measured at 55 °C with sweep rate 16–124 mV/s. Current peaks are detectable by double differentiation, indicating a diffusion limited charge transfer process. Two voltammogram self-crossing points between 0.3 and 5 V indicate an additional memristive effect [45]. (c) Nyquist plot of the complex impedance measured at room temperature with 354 mV, 1 MHz-500 μ Hz excitation voltage. The high frequency semi-circle was fit to a depressed circle with $R = 97.2 \pm 0.3 \text{ M}\Omega$ ($R_{\text{adj}} = 0.99989$). A Warburg constant phase (diffusion) element is observed at frequencies lower than 9mHz, consistent with the presence of ECM actuation in Fig. 2c-f. $\tan^{-1}(-Z_{\text{im}}/Z_{\text{real}}) \ll 45^\circ$, is characteristic of diffusion in a confined space [44]. (d) Peak current as a function of the square root of the sweep rate at 55 °C. Current asymmetry is observed between the positive and negative potential ranges and the behavior is non-linear. (e) Arrhenius-type plot of the diffusion coefficient measured between 25 and 100 °C (See Fig. S5 in Supplementary Information for temperature dependent cyclic voltammograms). Again, non-linearity is observed.

4.2. Niobium-based nanocomposite.

The structural characteristics of a Nb-oxide/20GDC composite are similar to those of the V oxide-based composites. The XRD pattern does not exhibit sharp diffraction peaks but rather broad diffraction features with the strongest maximum at $2\theta = 30 \pm 0.5^\circ$ and $\text{FWHM} > 5.8^\circ$ (Fig. 4a). SEM images reveal a dense crystalline structure with mean grain agglomerate size $52 \pm 6 \text{ nm}$ (Fig. 4b). The Nb K-edge XANES spectra (Fig. 4c) show that the position of the main absorption edge lies between that of Nb(0) and Nb(IV), *i.e.*, the average oxidation state of Nb is less

than +4. The R-space EXAFS profile (Fig. S2a) is dominated by a peak at $\sim 1.5 \text{ \AA}$, assigned to the Nb–O bond. In order to account for intrinsic, inelastic losses to the EXAFS amplitude, quantitative EXAFS analysis was performed on Nb foil to obtain an empirical reduction factor (0.76), (Fig. S2b and Table S1) that was then applied in fitting the spectrum of the Nb-oxide/20GDC composite (Fig. S2c and Table S2). According to the fitting results, the Nb–O bond length in the Nb-based composite is $2.09 \pm 0.03 \text{ \AA}$ (Table S2) and the coordination number is 3.9 ± 1.2 . Interestingly, in contrast to the V-oxide/20GDC composite, the Ce L₃-edge XANES spectrum of the Nb-based composite (Fig. S2d) reveals that

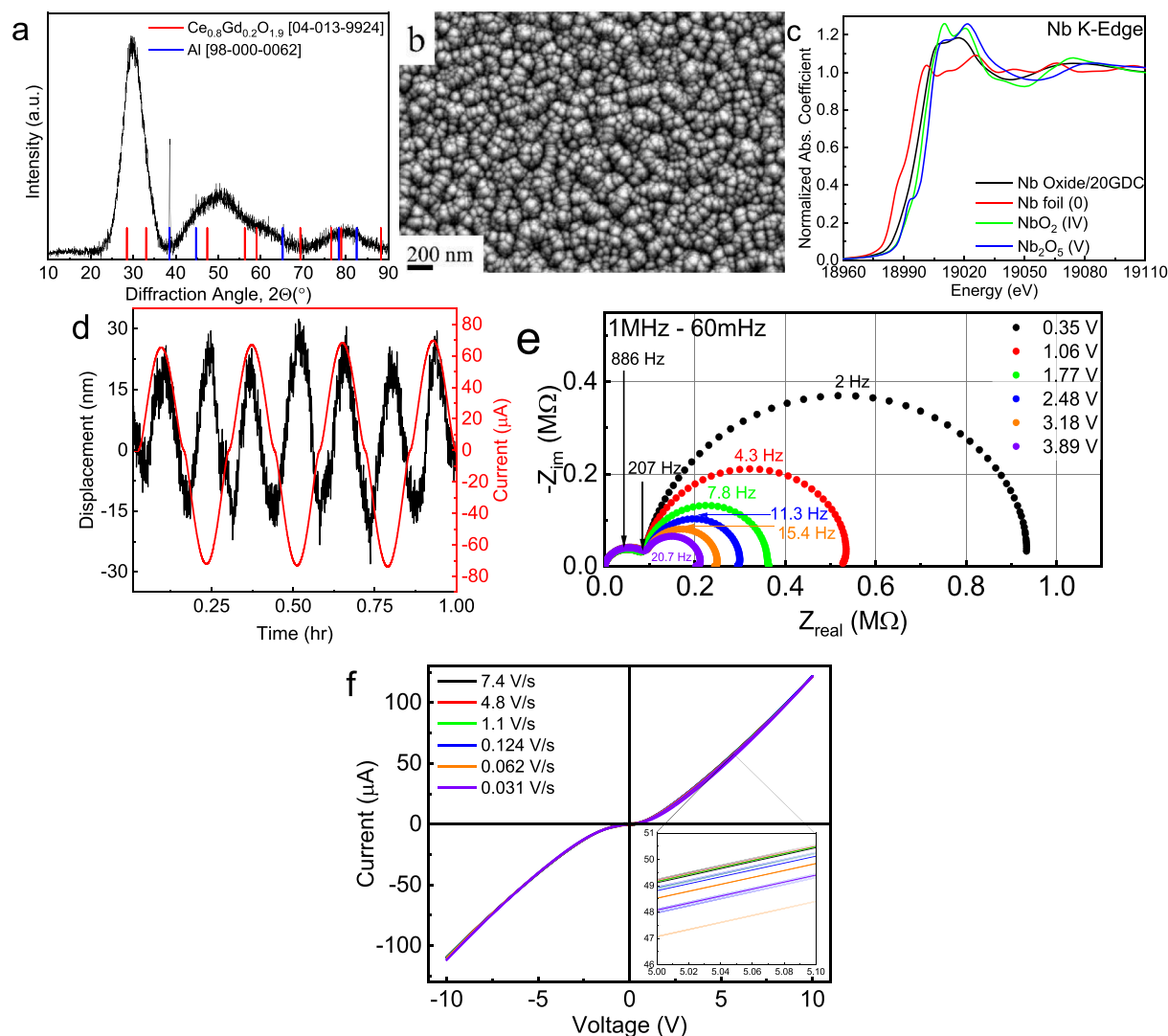


Fig. 4. Nb oxide/20GDC composite. (a) X-ray diffraction pattern, identifying nanocrystalline 20GDC (cf. Fig. 2a). (b) High resolution SEM micrograph of the composite layer deposited on a fused SiO_2 substrate. Aggregate feature size of 52 ± 6 nm was determined by the linear intercept method. (c) Nb K-edge XANES spectrum of the composite layer deposited on fused SiO_2 substrate. Spectra of Nb foil, NbO_2 , and Nb_2O_5 are shown for comparison. (d) Vertical displacement measured by custom-designed, auto-focusing optical technique [12] for Nb oxide/20GDC composite WB based devices driven at 8 V, 1 MHz; the measured current is also shown. Displacement was centered around zero by removing the background drift. Second harmonic response is demonstrated, consistent with electrostriction [43,47]. (e) Nyquist plot of the complex impedance of a Nb oxide/20GDC composite WB based device, measured at room temperature with 354 mV–3.8 V, 1 MHz–60 MHz excitation voltage. Significant dependence on voltage amplitude was observed for the lower frequency semi-circle, characteristic of blocking contact behavior. A Warburg constant phase (diffusion) element was not observed at low frequencies. (f) Cyclic voltammograms of a Nb oxide/20GDC composite WB based device measured at room temperature, sweep rates 7.4–0.031 V/s. Weak diode-like behavior, independent of sweep rate, was observed.

the oxidation states of Ce are dominated by +3, *i.e.*, cerium in the composite is heavily reduced.

Application of alternating voltage to the multilayer actuator with Nb oxide/20GDC composite WBs generates an electromechanical response at the second harmonic (Fig. 4d) for all frequencies investigated (0.5–20 Hz). Absence of a measurable first order response indicates that, if present, an ECM contribution to actuation is too small to be detected. A second harmonic electromechanical response can not be related to mass transfer: mass transfer reverses direction upon reversal in direction of the applied voltage. On the other hand, it is well known that Gd-doped ceria exhibits a strong electrostriction effect, *i.e.*, unidirectional material deformation with amplitude proportional to the square of the AC electric field, and with response at the second harmonic of the field frequency. If ionic transport is blocked, the electrostrictive deformation of Gd-doped ceria becomes dominant, even though it is small. This finding is consistent with the fact that a Nyquist plot (Fig. 4e) reveals two distinct circular arcs at high frequency, without the low frequency constant

phase element expected for diffusion-controlled processes. The higher frequency arc does not change with increase of the excitation voltage from 0.35 V to 3.89 V, while the radius of the lower frequency arc is reduced. Analysis of the lower frequency arc, given in Supplementary Section 10.4, suggests that it is related to a blocking layer at the electrical contact. This agrees with the fact that the I-V curves are symmetric and lack hysteresis, irrespective of sweep rate (Fig. 4f), indicating the absence of an electrochemical reaction.

4.3. Molybdenum based nanocomposite

Similar to V- and Nb-oxide composites, the XRD pattern of the Mo-oxide/20GDC composite does not contain sharp diffraction peaks. In addition to a broad maximum at $2\theta = 30 \pm 0.5^\circ$, estimated FWHM = $12 \pm 0.5^\circ$, there is a second maximum at $2\theta = 40.4 \pm 0.3^\circ$, estimated FWHM $> 11 \pm 0.3^\circ$ (Fig. 5a). The maxima cannot be assigned to a specific lattice symmetry. SEM images reveal dense, agglomerated

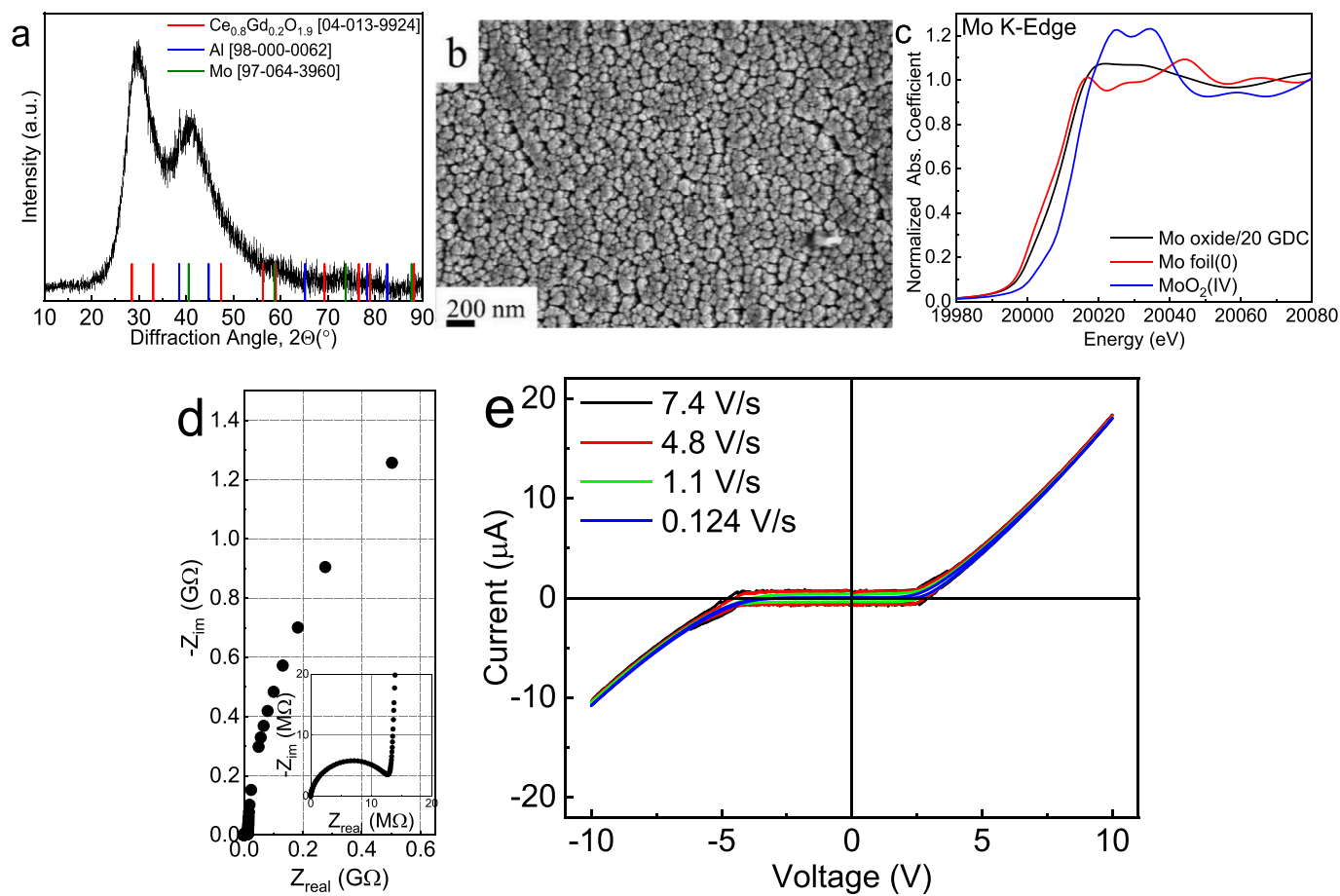


Fig. 5. Mo oxide/20GDC composite. (a) X-ray diffraction pattern. (b) High resolution SEM micrograph. Aggregate feature size of 60 ± 10 nm was determined by the linear intercept method. (c) Mo K-edge XANES spectrum measured on the composite layer deposited on fused SiO_2 substrate. Spectra of Mo metal foil and MoO_2 are shown for comparison. (d) Nyquist plot of the complex impedance measured for the Mo-oxide/20GDC composite WB based device operating at room temperature with 354 mV, 1 MHz-2MHz excitation voltage. The vertical line observed at low frequencies is indicative of a blocking contact. A Warburg constant phase (diffusion) element was not observed at low frequencies. (e) Cyclic voltammograms of Mo oxide/20GDC composite WB based device operating at room temperature with sweep rates 7.4–0.124 V/s. No dependence on sweep rate was observed; rather, a combined diode/resistor-type behavior was demonstrated, consistent with the blocking contact detected in (d). No ECM response was observed for Mo-oxide/20GDC composite based devices.

structures with feature size 60 ± 10 nm (Fig. 5b). The Mo K-edge XANES spectrum (Fig. 5c) shows that the position of the main absorption edge lies between that of Mo(0) and Mo(IV), while the Fourier transform magnitude of EXAFS reveals the presence of a second peak corresponding to a Mo–Mo pair, characteristic of Mo metal foil (Fig. S3a). As such, we conclude that following sputtering, the average oxidation state of Mo is intermediate between Mo(0) and Mo(IV). The EXAFS data of Mo foil were fit (Fig. S3b and Table S3) to obtain the amplitude reduction factor (0.82) which was then applied in fitting the spectrum of the Mo-oxide/20GDC composite (Fig. S3c and Table S4). In quantitative fitting analysis, it was found that two contributions are required in order to fit the EXAFS spectrum of the Mo-oxide/20GDC composite: Mo–O and Mo–Mo bonds. The Mo–Mo bond length in the Mo-based composite is 2.71 ± 0.04 Å (Table S3), which is very close to the length of the Mo–Mo bond (2.71 ± 0.01 Å) in Mo metal (Table S4). This indicates the presence of a Mo metallic phase and a $\text{Mo}^{\delta+}$ phase ($0 < \delta < 4$). The Ce L_3 edge XANES spectrum of the Mo-based composite (Fig. S3d) is dominated by Ce^{3+} , allowing us to conclude that the composite must contain metallic Mo, MoO_x , Gd_2O_3 and Ce_2O_3 . No mechanical response to applied voltage was detected for Mo-oxide based composite devices. Impedance spectroscopy demonstrated a high frequency arc and a partial arc appearing at low frequencies (Fig. 5d). The low frequency spectral features are similar to those reported earlier for blocking contacts (Ni or Cr) on 20GDC membranes ([43]). Cyclic voltammetry

demonstrates symmetric non-linear resistance lacking an opening at any sweep rate (Fig. 5e). Thus, electrical characterization supports the absence of electrochemical reactions at the electrodes.

4.4. Cu- and Ag-based nanocomposites

The XRD patterns of the Cu-based composite display diffraction peaks which may be indexed according to Cu_2O and 20GDC space groups (Fig. 6a). SEM images of Cu-oxide based composites show distinct phase segregation in the form of sub-micron sized particles (Fig. 6b). Similarly, the XRD pattern of the Ag-based composite reveals the presence of fully formed crystallites of metallic silver (Fig. 7a), arguing against the formation of a nanocrystalline composite and consistent with SEM imaging of micron-size features (Fig. 7b). The pre-edge shoulder of the Cu K-edge XANES spectrum lies between that of Cu_2O and CuO , but closer to Cu_2O , while the white line closely resembles that of CuO (Fig. 6c). The average oxidation state of Cu is therefore between +1 and +2. The second shell peak in the Cu EXAFS spectrum is very weak, characteristic of strong structural disorder in the local environment beyond the first shell (Fig. S4a). For Ag, both the XANES (Fig. 7c) and EXAFS (Fig. S4b) regions of the X-ray absorption coefficient show clear metallic character. The shape of the absorption edge and the R-space profile are very similar to those of bulk Ag. In both composites, Ce was found in oxidation state +4 (Fig. S4c). Since

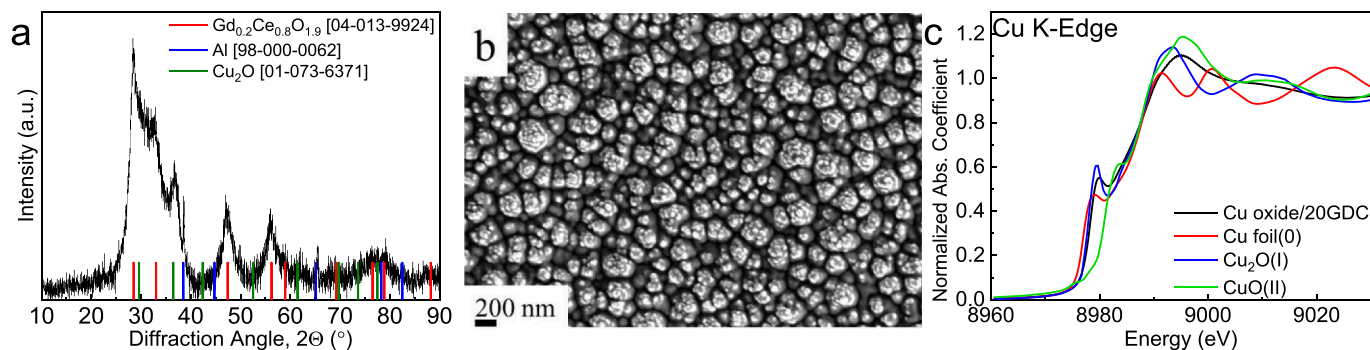


Fig. 6. Cu oxide/20GDC composite. (a) X-ray diffraction pattern. (b) High resolution SEM micrograph. (c) Cu K-edge XANES spectrum measured on the composite layer deposited on a fused SiO_2 substrate. Spectra of Cu metal foil, Cu_2O and CuO are also shown for comparison. The presence of the Cu_2O phase and a 5-fold increase in agglomerate size (245 ± 38 nm), as compared to the V oxide/20GDC composite, were observed in both (a) and (b). Due to phase segregation and increase in grain size, electrical/electromechanical characterizations were not performed on this composite.

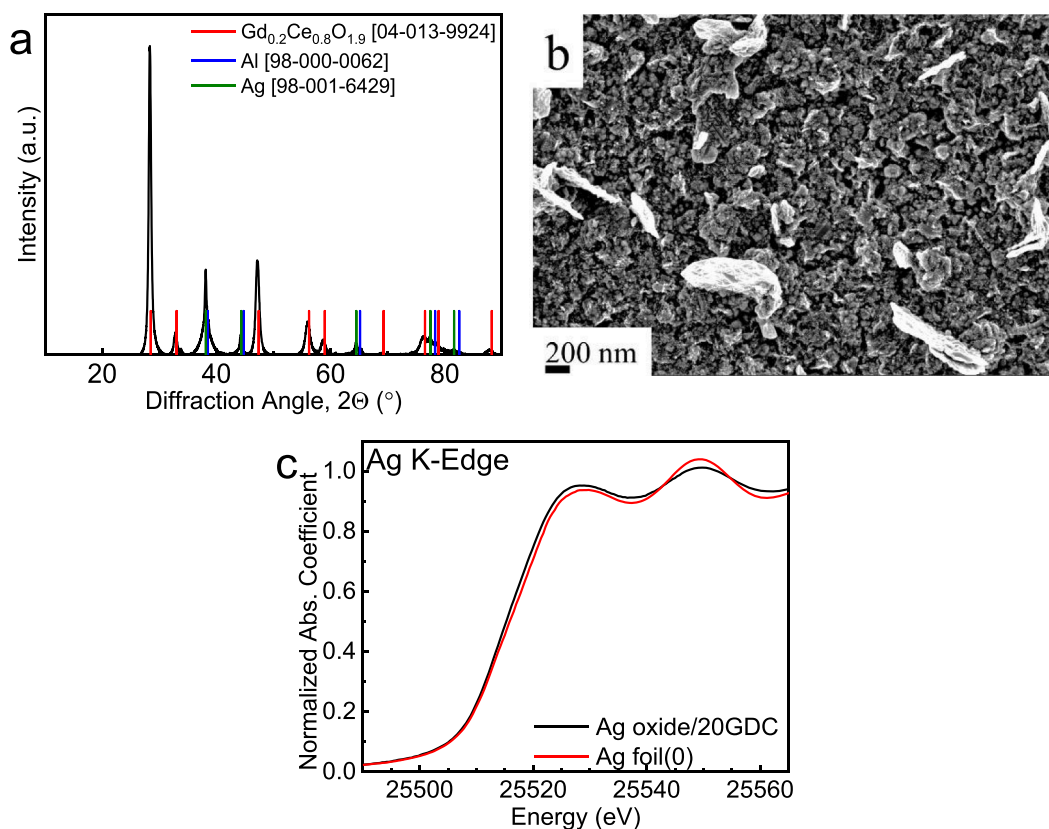


Fig. 7. Ag oxide/20GDC composite. (a) X-ray diffraction pattern. (b) High resolution SEM micrograph, (c) Ag K-edge XANES spectrum measured on the composite layer deposited on a fused SiO_2 substrate. Spectrum of silver metal foil is shown for comparison. Silver metal was observed in (a); the narrow peak width combined with the absence of Ag oxide diffraction indicate that a nanocomposite was not formed. Silver platelets are observed in (b). Due to obvious phase segregation, electrical/electromechanical measurements were not made on this composite.

nanocrystalline composites do not form with Ag and Cu, they were excluded from further consideration and no actuators based on these composites were prepared.

5. Discussion

We note that the metal-oxide/20GDC nanocomposites prepared for this report were deposited by magnetron sputtering under controlled conditions and the resulting stoichiometry corresponds to these conditions (Supplementary, Table 2). However, as our earlier work with WBs containing [Ti oxide/20CGO] demonstrated, significant changes in the

chemistry and structural characteristics of the WB must take place in order for a major improvement in ECM behavior to be observed. Consequently, the materials examined here should be viewed as representative cases, providing guidelines regarding the formation and suitability of nanocomposite WBs for ECM devices. Redox reactions, essential for ECM functioning, do not take place in the WBs containing Nb-, Mo- Cu- or Ag-oxides; yet the different chemistry of each these metals/metal oxides, places investigation of the possible reasons for the absence of such reactions beyond the scope of the current study. The most obvious conclusion drawn from the case of Cu and Ag is that semi-noble metals undergo segregation during co-sputtering with 20GDC,

either in the form of an oxide or in the form of a metal, rendering them unsuitable for ECM WBs. Co-sputtering of V, Nb or Mo with 20GDC does produce nanocomposites. However, as suggested by the lack of a low frequency, Warburg constant phase (diffusion) element in the Nyquist plots for Nb-oxide and Mo-oxide based composites (Fig. 4e and Fig. 5d), ECM actuation was not produced. For the Nb-oxide based composite WB, we suggest that its failure to produce ECM actuation is due to the formation of an insulating Nb-oxide phase, which once formed, inhibits any further electrochemical reaction. The difference in electromechanical behavior between Nb-oxide and Mo-oxide composite based WBs is related to the nature of the interface between the metal oxide and 20GDC, as is evident from the IS data. While TiO_x is conductive irrespective of stoichiometry, VO_x stoichiometry close to V_2O_5 results in poor conductivity. We may suggest that increasing the content of vanadium in a V-oxide based composite could shift the equilibrium towards lower oxidation states, possibly improving its suitability for WBs in ECM actuators.

6. Summary

Following the successful demonstration of a co-sputtered Ti oxide/20GDC nanocrystalline composite as a WB for ECM actuation, V-, Nb-, Mo-, Cu- and Ag-oxide based composites were examined as potential alternatives. We observed that Cu and Ag do not form nanocrystalline composites with 20GDC upon co-sputtering; rather, two separate phases are formed in each case, copper mixed oxide and silver metal, respectively. With respect to Mo, a nanocrystalline composite is present; but under voltage, no electromechanical response was detected. This can be tentatively explained by the Nyquist plot that shows that a blocking contact is formed. Also, in the case of Nb, a nanocomposite was formed but the actuator only produced second harmonic electrostrictive response. According to electrical characterization, the Nb-oxide composite does not appear to support an electrochemical reaction, likely because of a poorly conductive Nb phase that, once formed, cannot be reduced on a reasonable time scale, thereby blocking the interface.

Co-sputtered V oxide and 20GDC does produce a nanocrystalline composite, in which both vanadium and cerium are in mixed oxidation states, +4/+5 for V, +3/+4 for Ce. Chemically, the composite is therefore $VO_{2+x}/20GDC$. The ECM actuator built with this composite produces ECM response which is slower than previously demonstrated by the Ti oxide/20GDC WB based actuator. Cyclic voltammetry and impedance spectroscopy point to the presence of some memristive behavior in addition to the electrochemical reaction. This suggests that a poorly conductive phase is formed, blocking the interface, which may be related to the presence of V_2O_5 . If this is in fact correct, increase in the concentration of V in the composite should shift the chemical equilibrium away from the V_2O_5 phase thereby improving the performance of the working body. Successful demonstration of ECM actuation in a V-oxide based system, suggests that with nanocomposite WBs, ECM actuation is not unique for Ti-oxide, but is rather a more general phenomenon defined by compositional criteria. Importantly, the systematic survey presented above indicates that nanocrystalline composite WBs could play a significant role in the development of ecological, micro-electromechanical systems.

Author statement

Evgeniy Makagon, inception of the idea, development of the deposition processes, construction of the actuators, collection and analysis of the XRD data, electromechanical and electromechanical measurements, editing and data analysis.

Junying Li, collection and analysis of the XAS data.

Yuanyuan Li, collection and analysis of the XAS data.

Ellen Wachtel, analysis of the XRD and structural data, general guidance and editing.

Anatoly I. Frenkel, inception of the idea, collection and analysis of

the XAS data,

Igor Lubomirsky, inception of idea, general data analysis and coordination, mechanical analysis and editing.

Declaration of Competing Interest

None.

Acknowledgements

AIF, JL and YL acknowledge support by NSF Grant number DMR-1911592. IL acknowledges the NSF-BSF program grant 2018717. This research received funding from the Minerva Center for Self-Repairing Systems for Energy & Sustainability and it is made possible in part by the historic generosity of the Harold Perlman Family. This research used beamlines 8-ID (ISS) and 7-BM (QAS) of the National Synchrotron Light Source II, a U.S. DOE Office of Science User Facility operated for the DOE Office of Science by Brookhaven National Laboratory under Contract No. DE-SC0012704. This research used beamline 20-BM-B of the Advanced Photon Source, a U.S. (DOE) Office of Science User Facility operated for the DOE Office of Science by Argonne National Laboratory under Contract No. DE-AC02-06CH11357. AIF acknowledges support by a Weston Visiting Professorship during his stay at the Weizmann Institute of Science. IL and EM acknowledge Mr. Ilya Makagon for the graphical design of Fig. 1.

Appendix A. Supplementary data

Supplementary data to this article can be found online at <https://doi.org/10.1016/j.ssi.2022.115913>.

References

- [1] S.R. Bishop, D. Marrocchelli, C. Chatzichristodoulou, N.H. Perry, M.B. Mogensen, H.L. Tuller, E.D. Wachsman, *Annu. Rev. Mater. Res.* 44 (2014) 205, <https://doi.org/10.1146/annurev-matsci-070813-113329>.
- [2] S.R. Bishop, N.H. Perry, D. Marrocchelli, B.W. Sheldon, *Electro-Chemo-Mech. Solids* (2017) V, <https://doi.org/10.1007/978-3-319-51407-9>.
- [3] J.G. Swallow, W.H. Woodford, Y. Chen, Q. Lu, J.J. Kim, D. Chen, Y.M. Chiang, W. C. Carter, B. Yildiz, H.L. Tuller, K.J. Van Vliet, *J. Electroceram.* 32 (1) (2014) 3, <https://doi.org/10.1007/s10832-013-9872-2>.
- [4] L.Y. Beaulieu, K.W. Eberman, L.N. Turner, L.J. Krause, J.R. Dahn, *Electrochem. Solid-State Lett.* 4 (9) (2001) A137, <https://doi.org/10.1149/1.1388178>.
- [5] Y. Li, X. Cheng, Y. Zhang, K. Zhao, *Mater. Today Nano* 7 (2019), <https://doi.org/10.1016/j.mtnano.2019.100040>. Artn 100040.
- [6] Y. Qi, H.B. Guo, L.G. Hector, A. Timmons, *J. Electrochem. Soc.* 157 (5) (2010) A558, <https://doi.org/10.1149/1.3327913>.
- [7] V.A. Sethuraman, M.J. Chon, M. Shimshak, V. Srinivasan, P.R. Guduru, *J. Power Sources* 195 (15) (2010) 5062, <https://doi.org/10.1016/j.jpowsour.2010.02.013>.
- [8] Y. Zhao, P. Stein, Y. Bai, M. Al-Siraj, Y.Y.W. Yang, B.X. Xu, *J. Power Sources* 413 (2019) 259, <https://doi.org/10.1016/j.jpowsour.2018.12.011>.
- [9] S.R. Bishop, *Acta Mech. Sinica* 29 (3) (2013) 312, <https://doi.org/10.1007/s10409-013-0045-y>.
- [10] K.J. Zhao, M. Pharr, J.J. Vlassak, Z.G. Suo, *J. Appl. Phys.* 108 (7) (2010), <https://doi.org/10.1063/1.3492617>. Artn 073517.
- [11] J.G. Swallow, J.J. Kim, J.M. Maloney, D. Chen, J.F. Smith, S.R. Bishop, H.L. Tuller, K.J. Van Vliet, *Nat. Mater.* 16 (7) (2017) 749, <https://doi.org/10.1038/NMAT4898>.
- [12] E. Makagon, E. Wachtel, L. Houben, S.R. Cohen, Y.Y. Li, J.Y. Li, A.I. Frenkel, I. Lubomirsky, *Adv. Funct. Mater.* (2020), <https://doi.org/10.1002/Adfm.202006712>. Artn 2006712.
- [13] S.R. Wang, T. Kobayashi, M. Dokiya, T. Hashimoto, *J. Electrochem. Soc.* 147 (10) (2000) 3606, <https://doi.org/10.1149/1.1393946>.
- [14] E. Mishuk, A. Ushakov, E. Makagon, S.R. Cohen, E. Wachtel, T. Paul, Y. Tsur, V. Y. Shur, A. Kholkin, I. Lubomirsky, *Adv. Mater. Interfaces* 6 (6) (2019), <https://doi.org/10.1002/Admi.201801592>. Artn 1801592.
- [15] J. Garcia-Barriocanal, A. Rivera-Calzada, M. Varela, Z. Sefrioui, E. Iborra, C. Leon, S.J. Pennycook, J. Santamaria, *Science* 321 (5889) (2008) 676, <https://doi.org/10.1126/science.1156393>.
- [16] P. Heitjans, S. Indris, *Aust. J. Phys.* 15 (30) (2003) R1257, <https://doi.org/10.1088/0953-8984/15/30/202>.
- [17] S. Kim, J.S. Lee, C. Mitterbauer, Q.M. Ramasse, M.C. Sarahan, N.D. Browning, H. J. Park, *Chem. Mater.* 21 (7) (2009) 1182, <https://doi.org/10.1021/cm801584e>.
- [18] N. Sata, K. Eberman, K. Eberl, J. Maier, *Nature* 408 (6815) (2000) 946, <https://doi.org/10.1038/35050047>.

- [19] S. Surnev, M.G. Ramsey, F.P. Netzer, *Prog. Surf. Sci.* 73 (4–8) (2003) 117, <https://doi.org/10.1016/j.progsurf.2003.09.001>.
- [20] S. Kachi, T. Takada, K. Kosuge, *J. Phys. Soc. Jpn.* 18 (12) (1963) 1839, <https://doi.org/10.1143/jpsj.18.1839>.
- [21] A. Foroughi-Abari, K.C. Cadien, *Thin Solid Films* 519 (10) (2011) 3068, <https://doi.org/10.1016/j.tsf.2010.12.036>.
- [22] R.A. Rani, A.S. Zoolfakar, A.P. O'Mullane, M.W. Austin, K. Kalantar-Zadeh, *J. Mater. Chem. A* 2 (38) (2014) 15683, <https://doi.org/10.1039/c4ta02561j>.
- [23] A.M. Al-Baradi, M.M. El-Nahass, A.M. Hassanien, A.A. Atta, M.S. Alqahtani, A. O. Aldawsari, *Optik* 168 (2018) 853, <https://doi.org/10.1016/j.ijleo.2018.05.020>.
- [24] S.L. Fernandes, L.G.S. Albano, L.J. Affonco, J.H.D. da Silva, E. Longo, C.F.D. Graeff, *Front. Chem.* 7 (2019), <https://doi.org/10.3389/fchem.2019.00050>. Artn 50.
- [25] M.P.F. Graca, M. Saraiva, F.N.A. Freire, M.A. Valente, L.C. Costa, *Thin Solid Films* 585 (2015) 95, <https://doi.org/10.1016/j.tsf.2015.02.047>.
- [26] L. Kihlborg, *Acta Chem. Scand.* 13 (5) (1959) 954, <https://doi.org/10.3891/acta.chem.scand.13-0954>.
- [27] J.M. Pachthofer, C. Jachs, R. Franz, E. Franzke, H. Kostenbauer, J. Winkler, C. Mitterer, *Vacuum* 131 (2016) 246, <https://doi.org/10.1016/j.vacuum.2016.07.002>.
- [28] J. Bullock, A. Cuevas, T. Allen, C. Battaglia, *Appl. Phys. Lett.* 105 (23) (2014), <https://doi.org/10.1063/1.4903467>. Artn 232109.
- [29] S. Chuang, C. Battaglia, A. Azcatl, S. McDonnell, J.S. Kang, X.T. Yin, M. Tosun, R. Kapadia, H. Fang, R.M. Wallace, A. Javey, *Nano Lett.* 14 (3) (2014) 1337, <https://doi.org/10.1021/nl4043505>.
- [30] Y.F. Shi, B.K. Guo, S.A. Corr, Q.H. Shi, Y.S. Hu, K.R. Heier, L.Q. Chen, R. Seshadri, G.D. Stucky, *Nano Lett.* 9 (12) (2009) 4215, <https://doi.org/10.1021/nl902423a>.
- [31] J. Meyer, S. Hamwi, M. Kroger, W. Kowalsky, T. Riedl, A. Kahn, *Adv. Mater.* 24 (40) (2012) 5408, <https://doi.org/10.1002/adma.201201630>.
- [32] B. Purusottam-Reddy, K. Sivajee-Ganesh, K. Jayanth-Babu, O.M. Hussain, C. M. Julien, *Ionics* 21 (8) (2015) 2319, <https://doi.org/10.1007/s11581-015-1403-5>.
- [33] V.F. Drobny, D.L. Pulfrey, *Thin Solid Films* 61 (1) (1979) 89, [https://doi.org/10.1016/0040-6090\(79\)90504-2](https://doi.org/10.1016/0040-6090(79)90504-2).
- [34] A. Parretta, M.K. Jayaraj, A. DiNocera, S. Loreti, L. Quercia, A. Agati, *Phys. Stat. Sol. A* 155 (2) (1996) 399, <https://doi.org/10.1002/pssa.2211550213>.
- [35] B. Pecquenard, F. Le Cras, D. Poinot, O. Sicardy, J.P. Manaud, A.C.S. Appl. Mater. Interfaces 6 (5) (2014) 3413, <https://doi.org/10.1021/am4055386>.
- [36] G. Mahendra, R. Malathi, S.P. Kedhareswara, A. Lakshmi-Narayana, M. Dhananjaya, N. Guruprakash, O.M. Hussain, A. Mauger, C.M. Julien, *Appl. Nano 2* (1) (2021) 46, <https://doi.org/10.3390/applnano2010005>.
- [37] J.F. Pierson, C. Rousselot, *Surf. Coat. Technol.* 200 (1–4) (2005) 276, <https://doi.org/10.1016/j.surfcoat.2005.02.005>.
- [38] S.B. Rivers, G. Bemhardt, M.W. Wright, D.J. Frankel, M.M. Steeves, R.J. Lad, *Thin Solid Films* 515 (24) (2007) 8684, <https://doi.org/10.1016/j.tsf.2007.03.139>.
- [39] E. Makagon, S. Khodorov, A. Frenkel, L. Chernyak, I. Lubomirsky, *Opt. Eng.* 60 (12) (2021), 124112, <https://doi.org/10.1117/1.OE.60.12.124112>.
- [40] S. Deshpande, S. Patil, S.V.N.T. Kuchibhatla, S. Seal, *Appl. Phys. Lett.* 87 (13) (2005), <https://doi.org/10.1063/1.2061873>. Artn 133113.
- [41] J. Li, Y. Li, P.K. Routh, E. Makagon, I. Lubomirsky, A.I. Frenkel, *J. Synchrotron Radiat.* 28 (2021) 5.
- [42] A.I. Frenkel, Y. Feldman, V. Lyahovitskaya, E. Wachtel, I. Lubomirsky, *Phys. Rev. B* 71 (2005) 2, <https://doi.org/10.1103/PhysRevB.71.024116>.
- [43] E. Mishuk, E. Makagon, E. Wachtel, S.R. Cohen, R. Popovitz-Biro, I. Lubomirsky, *Sens. Actuat. A* 264 (2017) 333, <https://doi.org/10.1016/j.sna.2017.07.047>.
- [44] A.J. Bard, L.R. Faulkner, J. Leddy, C.G. Zoski, *Electrochemical Methods: Fundamentals and Applications*, Wiley New York, 1980.
- [45] R. Schmitt, J. Spring, R. Korobko, J.L.M. Rupp, *ACS Nano* 11 (9) (2017) 8881, <https://doi.org/10.1021/acsnano.7b03116>.
- [46] Q.Y. Lu, S.R. Bishop, D. Lee, S. Lee, H. Bluhm, H.L. Tuller, H.N. Lee, B. Yildiz, *Adv. Funct. Mater.* 28 (34) (2018), <https://doi.org/10.1002/Adfm.201803024>. Artn 1803024.
- [47] N. Yavo, O. Yehekel, E. Wachtel, D. Ehre, A.I. Frenkel, I. Lubomirsky, *Acta Mater.* 144 (2018) 411, <https://doi.org/10.1016/j.actamat.2017.10.056>.